Available online at www.HighTechJournal.org

HighTech and Innovation Journal

ISSN: 2723-9535

Vol. 7, No. 1, March, 2026

Aerodynamics Analysis of a Novel Multirotor Structure Derived from Generative Design Using Computational Fluid Dynamics

Sane Souvanhnakhoomman [1*], Alvin Y. Chua [1]

[1] *Department of Mechanical Engineering, De La Salle University, 2401 Taft Ave, Malate, Manila 1004, Philippines.*

Received 12 November 2025; Revised 03 February 2026; Accepted 09 February 2026; Published 01 March 2026

Abstract

This study investigates whether generative design structures can enhance the aerodynamic efficiency and payload capacity of multirotor UAVs compared with conventional stacked-rotor layouts. The methodology integrated structural generative design in Autodesk Fusion 360 and evaluated hover aerodynamics using computational fluid dynamics (CFD) analysis in SimScale, employing a steady, pressure-based incompressible RANS solver and Multiple Reference Frame (MRF) zones to model hover at 4500 rpm. Three configurations were evaluated: a baseline "Initial Model" and two generative-design outcomes (Model 1 and Model 3). The results show that Model 1 provides negligible improvement, whereas Model 3 increases total thrust to 42.36 N, corresponding to a 9.6% gain relative to the initial configuration, and raises the system-average figure of merit by approximately 65%. Flow-field analyses indicate that Model 3 promotes cleaner inflow to the upper tier and a more coherent downwash, with reduced recirculation and interference-related losses. The novelty lies in coupling generative structural synthesis with CFD-based aerodynamic screening to demonstrate that frame geometry can actively enhance stacked-rotor hover performance.

Keywords: Multirotor UAV; Generative Design; CFD; Aerodynamic Interference; Thrust Performance; Aerodynamic Coefficient.

1. Introduction

Multirotor unmanned aerial vehicles (UAVs) are widely used in inspection, mapping, logistics, and public-safety missions because they provide precise control, compact operation, and reliable hover performance [1]. As payload demands and endurance targets increase, designers often adopt multi-layer or stacked rotor layouts to raise total thrust without substantially enlarging the vehicle footprint [2]. However, stacking rotors introduces strong aerodynamic interference: the wake of an upstream rotor alters the inflow to downstream rotors, reshaping induced velocity, swirl, and turbulence levels. This interaction can lead to thrust imbalance, increased power demand, and reduced hover efficiency [3, 4].

A substantial body of research has investigated rotor aerodynamics and interaction effects using experimental, analytical, and computational approaches. Geometric and operational parameters—including vertical spacing, relative rotor alignment (index angle), rotation direction, and local blockage—are known to influence wake ingestion and the thrust split between upper and lower rotors in closely spaced configurations [5, 6]. The lower rotor often operates in a degraded inflow environment because it ingests the contracted wake of the upper rotor, which modifies blade loading and can reduce the thrust-to-power ratio unless carefully tuned [7]. For modelling and design screening, steady Reynolds-Averaged Navier–Stokes (RANS) simulations coupled with the Multiple Reference Frame (MRF) method are commonly

* Corresponding author: sane_souvanhnakhoomman@dlsu.edu.ph

https://doi.org/10.28991/HIJ-2026-07-01-01

used to predict time-averaged hover loads, while URANS/LES approaches are typically applied when resolving transient wake structures and detailed turbulence dynamics is required [8].

Prior work also demonstrates that vehicle geometry can affect aerodynamic performance through its influence on local flow structures. Winglet optimization studies have shown that relatively small geometric changes can reduce induced losses and improve endurance or power requirements by reshaping vortex behavior [9, 10]. Propeller modelling across hover and forward flight further highlights the need for realistic assumptions when predicting thrust and torque, particularly when extending hover-based formulations to other regimes [11]. From a CFD-methodology perspective, studies employing k–ε turbulence modelling and SIMPLE pressure–velocity coupling illustrate practical approaches for obtaining stable solutions in wake-dominated flows [12, 13]. In addition, duct and ducted-propeller investigations confirm that surrounding structures can alter induced-velocity characteristics and overall aerodynamic behavior [14].

For multirotors, configuration-level geometry is particularly important. A parametric CFD study on a hexacopter showed that arm-angle arrangements can reshape rotor inflow by modifying blockage and vortex shedding near hub–arm junctions, thereby influencing thrust uniformity, induced losses, and passive stabilizing forces in hover. Guided by these findings, the present work adopts a connecting-arm layout informed by prior designs [15] to provide a consistent baseline for comparing the initial configuration with two generative-design candidates (Model 1 and Model 3). Propulsion-focused literature likewise emphasizes coupled aero-structural constraints: finite-element studies demonstrate how diameter and rotational speed increase aerodynamic and centrifugal loading and may elevate vibration risk if stiffness and damping are not considered [16]. Coaxial studies show that downstream rotors operate under degraded inflow and can recover efficiency through pitch tuning, improving thrust-to-power ratio [17]. Octocopter CFD investigations further indicate that rotor arrangement and interference can produce substantial differences in thrust capability at comparable power [18]. Complementary studies on blade-shape refinement and operating-point selection report efficiency gains under geometric constraints and across RPM ranges [19, 20], while propeller tests also show that thrust and tonal features can be sensitive to operating conditions and propeller properties [21].

In parallel, generative design has become a practical tool for producing lightweight UAV frames that satisfy structural objectives and manufacturing constraints, typically evaluated in terms of mass reduction, stiffness, and improvements in safety factor [22–24]. Most generative design workflows prioritize structural feasibility and treat aerodynamics as a post-design check rather than an integrated objective. This creates a clear research gap: it remains insufficiently understood how structurally optimized generative design frames influence rotor inflow quality, wake development, and interference-driven efficiency losses in stacked multirotor hover. In other words, a frame may be structurally excellent while unintentionally exacerbating rotor-rotor interference through local blockage, flow redirection, or wake confinement near the rotor discs.

To address this gap, the present study evaluates a two-layer (stacked) octocopter architecture derived from generative design and quantifies its hover aerodynamics using Computational Fluid Dynamics (CFD). A reproducible workflow is implemented: (i) define the stacked-rotor configuration and candidate frame geometries; (ii) apply steady incompressible RANS with MRF rotating zones under consistent operating conditions; (iii) compute rotor-level and total performance metrics (thrust, torque, coefficient thrust, coefficient power, and figure of merit); and (iv) interpret the observed trends using velocity and pressure fields to explain tier-wise interference and power usage. By holding the propulsion set constant across the baseline and generative-design candidates, the study isolates how structural geometry and rotor placement influence aerodynamic efficiency, rather than conflating changes in propeller design or control settings.

Accordingly, the objectives and contributions of this work are to: (i) introduce a novel stacked octocopter frame derived from generative design and report its key geometric parameters; (ii) establish a reproducible CFD methodology for multirotor interference assessment, including domain definition, meshing strategy, modelling assumptions, and convergence controls; and (iii) quantify thrust distribution and efficiency trends across the baseline and selected generative-design candidates, linking flow-field features to rotor–rotor interference mechanisms and providing configuration-level guidance for practical multirotor UAV design. The novelty lies in coupling structurally driven generative design with CFD-based aerodynamic screening to produce first principles evidence of how frame geometry reshapes stacked-rotor hover performance in terms of thrust, power, and efficiency.

2. Research Methodology

The study workflow is depicted schematically in Figure 1. The methodology for computational fluid dynamics (CFD) analysis of the aerodynamics of a new multirotor structure involves generating a traditional configuration octocopter in Generative design using generative AI, then selecting model outcomes, designing propellers and assembly a new model, rendering a mesh, setting boundary conditions and fluid properties, configuring the solver, running simulations, post-processing the results, validating against experimental data, optionally optimizing the design, documenting the process, and concluding the analysis. This structured approach ensures a thorough examination of the propeller's aerodynamic performance, aiding in design optimization and performance enhancement.

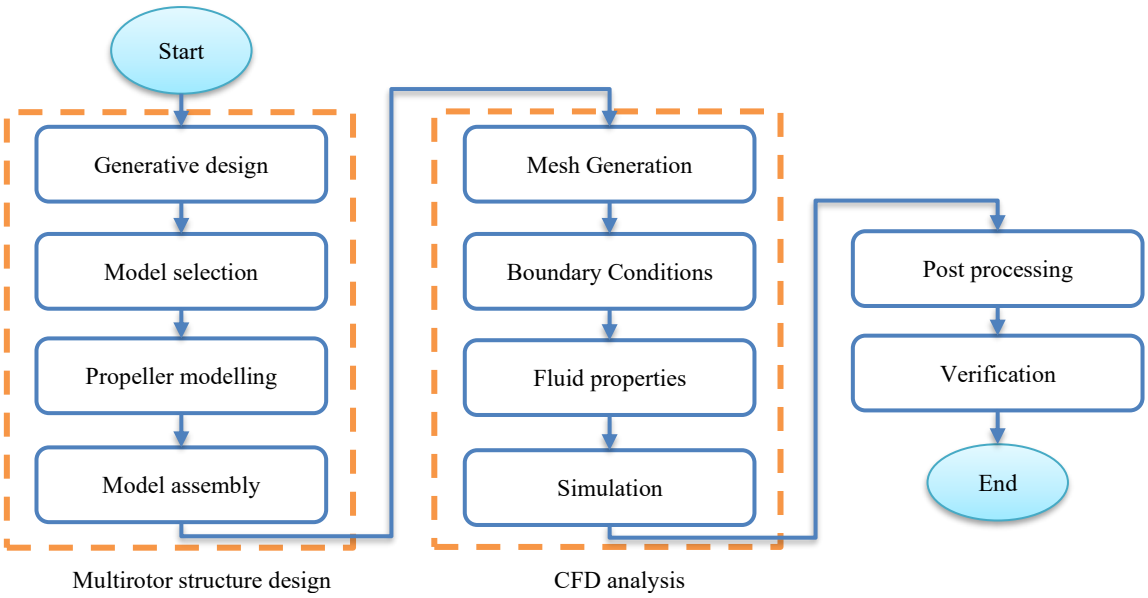

Figure 1. Overview of the design of a new multirotor structure and computational fluid dynamics analysis of the aerodynamics

2.1. Generative Design

In this study, a stacked two-layer octocopter is adopted as the reference platform to reduce structural weight, improve aerodynamic performance, and enhance payload capability. The initial octocopter frame shown in Figure 2 is adapted from the configuration proposed by Zhu et al. [25]. For the present work, the baseline geometries and key parameters from Zhu et al. [25] were adjusted to define a new octocopter frame that is compatible with the generative design workflow in Autodesk Fusion 360. The overall stacked two-layer architecture with four rotors per layer was retained, while the plate dimensions, arm lengths, and component locations were refined, considering electronic components and realistic manufacturing constraints. This refined configuration was then used as the starting point for the generative design process, in which material distribution and load paths were optimized without altering the propulsion layout, enabling a structurally efficient frame tailored for the subsequent aerodynamic assessment. Our configuration adopts a stacked layout with two rotor decks; each deck carries four rotors, giving eight in total on eight arms. The central top plate measures 370 mm along its centerline, the gap between the two decks is 200 mm, and the arm lengths of 500 mm for the upper and lower assemblies.

Figure 2. The initial octocopter frame was used as the baseline for the generative design process

We carried out the generative-design work in Autodesk's Fusion 360. In most industrial settings, tool access is limited by licenses and integration constraints rather than an unlimited software stack [26], so concentrating the workflow in as few applications as possible reduces hand-offs and conversion errors. Fusion 360's integrated environment covering CAD, generative-design exploration, and downstream model preparation allowed us to complete modeling, option ranking, and export within a single platform. This consolidation simplified version control and ensured consistent geometry across subsequent analysis steps.

Integrating generative design into the multirotor airframe followed a structured, constraint-driven setup. First, a baseline CAD model of the octocopter was created, and the key hardware interfaces, including the motor mounts, central hubs, and avionics locations, were defined as fixed references that the optimizer could not modify. Keep-out regions were then defined to prevent material growth around wiring paths and controller clearances, while bolt holes at the motor pads were locked using positional constraints. Representative loads were applied to emulate hover thrust and bounded

maneuver cases, ensuring that candidate frames were evaluated under realistic service conditions. The design brief specified ABS as the material [27] and enabled multiple manufacturing routes, including unrestricted, additive, and subtractive (milling), so the solver could explore viable load paths without violating process constraints. The objective was mass minimization subject to stiffness and strength requirements, and candidate geometries were generated and ranked in Autodesk Fusion 360.

In this study, no explicit flow-based objectives or aerodynamic constraints were imposed during the optimization stage. Instead, aerodynamic performance was evaluated post-design using CFD to quantify rotor–rotor interference, thrust distribution, and hover efficiency under identical operating conditions. The generative run produced thirty candidate frames over several optimization cycles. From this pool, eight ABS-based concepts met our constraints most convincingly and advanced to detailed review. These shortlisted geometries are presented in Table 1.

Table 1. Generative design outcomes of ABS plastic

Output	Model output	Max Von-Mises stress (MPa)	Max displacement global (mm)	Volume (mm^3)	Mass (kg)	Min factor of safety	Manufacturing method
5		0.637	0.431	8.939e+6	9.475	31.415	Additive manufacturing (AM)
3		0.491	0.449	6.337e+6	6.76	40.737	Additive manufacturing (AM)
6		0.775	0.65	8.641e+6	9.159	25.803	Additive manufacturing (AM)
8		1.97	2.209	8.373e+6	8.876	10.152	Additive manufacturing (AM)
10		2.001	2.389	8.600e+6	9.116	9.993	Additive manufacturing (AM)
3		2.001	2.389	9.165e+6	9.715	9.992	Additive manufacturing (AM)
4		0.874	0.774	7.615e+6	8.072	22.862	Additive manufacturing (AM)
1		0.490	0.448	6.010e+6	6.371	40.737	Additive manufacturing (AM)

From the candidates in Table 1, we down-selected two frames for detailed aerodynamic evaluation to ground-truth the generative outcomes. The initial down-selection was primarily structural, based on mass, peak von Mises stress, and maximum displacement under the prescribed load cases. Model 1 was chosen as the lightweight option, with a mass of 6.371 kg, a maximum von Mises stress of 0.490 MPa, and a maximum displacement of 0.448 mm. Model 3 served as a comparative design with similarly strong structural figures, namely a mass of 6.76 kg, stress of 0.491 MPa, and displacement of 0.449 mm. To reduce the risk of selecting structurally strong designs that could unintentionally degrade rotor inflow, the shortlisted candidates were also checked qualitatively for aerodynamic plausibility, with preference given to geometries that preserved rotor-disc clearance and minimized blockage in the expected downwash paths. Using Models 1 and 3, we conducted the CFD campaign shown in Figure 3, examining velocity fields, wake structures, pressure distributions, and force balances. Thrust production and power demand were compared using consistent operating conditions, and non-dimensional metrics (thrust coefficient, power coefficient, and figure of merit) were extracted to identify the more aerodynamically efficient configuration.

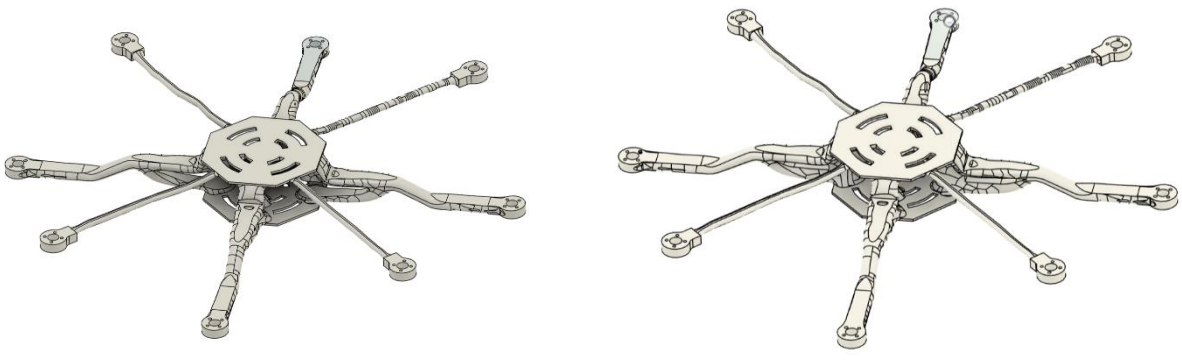

(a) (b)

Figure 3. The optimal generative design outcomes selected for aerodynamic analysis: (a) Model 1 (6.371 kg) and (b) Model 3 (6.76 kg)

2.2. Geometric Configurations for Analysis

This study performs a comparative aerodynamic analysis on three distinct, fully-assembled octocopter geometries, which are all depicted in Figure 4. To ensure a valid aerodynamic comparison, all three frame configurations were simulated using an identical set of eight propellers. Each propeller was modeled as a two-bladed rotor based on the NACA 4412 airfoil profile. The propellers have a diameter of 457.2 mm (18 in) and a nominal pitch of 177.8 mm (7 in). The first configuration is the initial traditional octocopter as shown in figure 4a, which serves as the baseline model and features a conventional. The other two configurations are the mass-optimized generative design outcomes, Model 1 in Figure 4(b) and Model 3 in Figure 4(c). Both generative variants use the same stacked layout: four rotors are mounted on the upper deck and four on the lower. The airframe measures 1,376 mm in overall length, and the two decks are spaced 120 mm apart, as illustrated in Figure 5. These fully defined assemblies, frame plus identical propellers, form the geometry set used for the CFD comparisons that follow.

(a) (b) (c)

Figure 4. The three configurations used for comparative CFD analysis: (a) the Initial configuration, (b) Generative Design Model 1, and (c) Generative Design Model 3

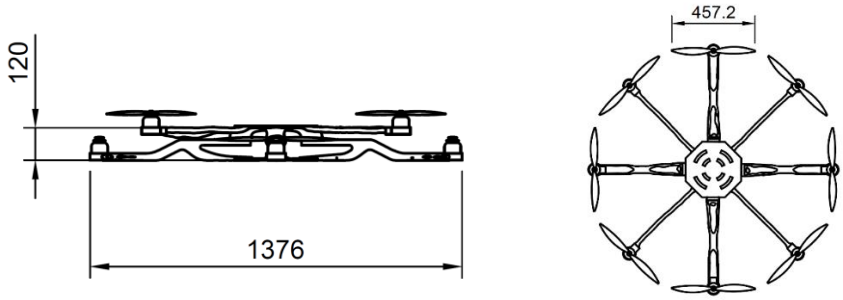

Front view Top view

Figure 5. Geometry configuration of model 1 and model 3

3. Computational Fluid Dynamics

We analyzed all three octocopter configurations using computational fluid dynamics, treating hover in a quiescent atmosphere. The aim was to characterize how each airframe shapes the surrounding flow, specifically the pressure field, local velocity distribution, and wake structure under identical operating conditions. For both the generative designs and the initial baseline, we extracted maps of pressure and velocity, examined mixing in the inter-rotor region, and quantified the induced-velocity plume beneath the eight rotors. These diagnostics reveal the principal aerodynamic effects of the stacked layout and allow a fair comparison of configurations [28-30].

3.1. Theoretical Approach and Physical Basis

In Stacked (two-layer) multirotor configurations operating in hover, the upper rotor induces a downward flow that contracts into a wake with increased axial velocity and swirl. The lower rotor, therefore, operates in a non-uniform, degraded inflow environment, which modifies blade loading and can reduce aerodynamic efficiency relative to an isolated rotor. The severity of this interference depends on geometric and operational parameters (e.g., vertical spacing, alignment/index angle, rotation direction) and on nearby structural blockage, which can further distort inflow and wake mixing. To interpret and compare designs consistently, the present study uses standard non-dimensional performance coefficients derived from momentum and similarity principles. The thrust and power coefficients are defined as shown in Equations 1 and 2 [7]:

$$C_T = \frac{T}{\rho n^2 D^4} \quad (1)$$

$$C_P = \frac{P}{\rho n^3 D^5} \quad (2)$$

where, T is thrust, P is shaft power, ρ is air density, n is rotational speed (rev/s), and D is rotor diameter. Hover efficiency is represented using the figure of merit (FM), which compares ideal induced power to actual power consumption [7]:

$$FM = \frac{C_T^{3/2}}{\sqrt{2}C_P} \quad (3)$$

3.2. Computational Domain and Boundary Conditions

To ensure a valid and direct comparison between the three different frame geometries (initial traditional, model 1, and model 3), an identical computational setup was applied to each. All CFD simulations were conducted in SimScale, a cloud-based computational platform, employing the steady, pressure-based incompressible RANS solver with the SIMPLE algorithm [31-33]. To capture the rotodynamic effects of each propeller, Multiple Reference Frame (MRF) rotating zones were assigned to all eight rotors. The steady RANS–MRF formulation was selected because this study aims to compare time-averaged hover performance across multiple frame configurations under identical operating conditions. This approach efficiently predicts mean induced flow and rotor-integrated metrics (thrust, torque, thrust coefficient, power coefficient, and figure of merit), enabling consistent screening and ranking of designs. Resolving phase-dependent wake dynamics would require URANS or LES at substantially higher computational cost and is beyond the scope of this comparative, time-averaged hover study. Therefore, unsteady simulations are reserved for future work.

The working fluid was set as air with properties corresponding to 25°C, namely a density (ρ) of 1.184 kg/m³ and a dynamic viscosity (μ) of 1.85×10^{-5} Pa·s. Each of the three octocopter models was individually placed within an identical computational domain, modelled as a rectangular virtual wind tunnel measuring 5000 mm, 5000 mm, and 8000 mm (x, y, and z directions, respectively). For its respective simulation, each octocopter model was positioned centrally in the lateral and vertical axes and 4000 mm downstream of the inlet, ensuring a clearance of 3-5 rotor diameters from all far-field boundaries to minimize wall-induced blockage effects. To capture the rotodynamic effects of the propellers. We modelled the rotor aerodynamics using MRF regions applied to all eight propellers in each configuration. For every propeller, the rotating control volume was a cylindrical sleeve 600 mm in diameter and 50 mm in axial depth, which provided a robust coupling between the rotating zone and the surrounding stationary flow field [34].

The same boundary conditions were applied to all three simulations to represent a steady hovering condition, as illustrated in Figure 6. The inlet boundary on the upstream face was prescribed as a velocity inlet with zero free-stream speed, representing still air. The downstream boundary was a pressure outlet fixed at zero gauge pressure so the wake could discharge without inducing backflow. To avoid artificial confinement, the sidewalls together with the top and bottom faces were set as symmetry planes, approximating an open atmosphere. Solid surfaces of the airframe and blades were treated as no-slip walls to capture realistic shear and pressure loads. Coupling between each rotor's MRF region and the surrounding stationary fluid was handled through dedicated interfaces to ensure proper momentum transfer. Every rotor operated as a rotating reference frame at 4,500 revolutions per minute (471.24 rad s^{-1}), with spin directions alternating according to the X8 pattern to balance torque and maintain symmetric thrust.

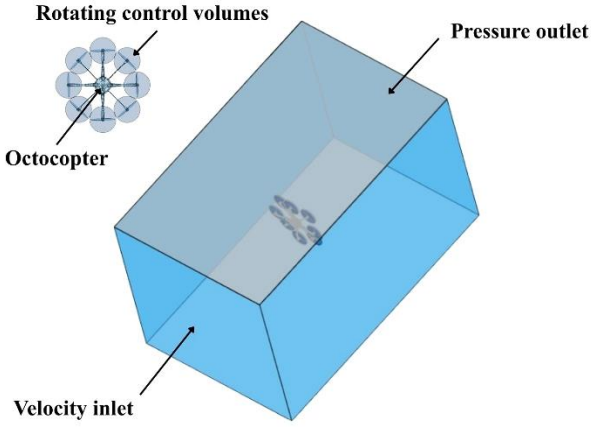

Figure 6. The standardised computational domain and boundary conditions

3.3. Meshing Strategy and Grid Independence Study

The computational mesh was generated in SimScale with the polyhedral hex-core (standard) mesher, which blends a hexahedral core with polyhedral cells around geometry to balance accuracy and cost. The grid structure is illustrated in Figure 7. Global sizing was set to automatic, and physics-based meshing was enabled. From the medium grid onward, automatic boundary layers were activated on the propeller blades and airframe to improve near-wall resolution while retaining a wall-function treatment. Local resolution was increased inside each MRF rotating sub-volume and on the blade/hub surfaces to better capture pressure and velocity gradients (tip-vortex/induction), whereas the far-field was kept coarser to reduce cell count. Eight non-overlapping MRF regions (one per rotor) were embedded in the single fluid body, yielding conformal interfaces between rotating and stationary regions for smooth transfer of velocity and pressure [35].

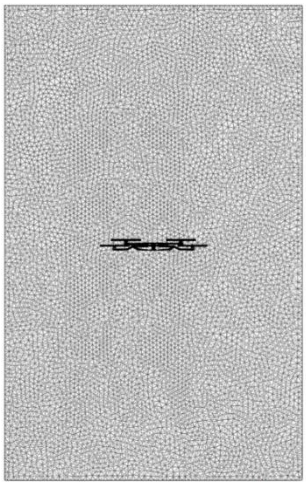

Figure 7. Discretised structure of the entire computational model

In Table 2, three meshes are shown to have been evaluated, with cell counts reported as the number of volumes. Due to the differences in geometric complexity, the final cell counts were 8.663 × 106 for the Initial Model, 6.807 × 106 for Model 1, and 7.885 × 106 for Model 3. All three meshes were generated using a hex-dominant polyhedral method. The mesh quality remained high across all cases, with an average orthogonal quality above 0.81 and a maximum skewness below 0.09, thereby meeting all standard RANS guidelines for this aerodynamic analysis.

Table 2. Mesh Statistics and Quality Parameters

Mesh Case	Element Count (×10⁶)	Avg Orthogonal Quality	Max Skewness	Cell Type	Solver Used
Initial model	8.663	0.83	0.09	Polyhedral (hex-core)	RANS (SIMPLE)
Model 1	6.807	0.81	0.07	Polyhedral (hex-core)	RANS (SIMPLE)
Model 3	7.885	0.832	0.08	Polyhedral (hex-core)	RANS (SIMPLE)

To verify numerical accuracy, a grid-independence check was performed with three mesh configurations as shown in Figure 8. Using the same steady RANS (SIMPLE) + MRF setup at 4500 RPM, per-rotor total forces and moments (pressure + viscous) were recorded every iteration, and steady values were taken as the mean of the last 20% of samples. The initial model predicted a total thrust of 38.6568 N. Model 1 yielded 38.16 N, a 1.29% decrease relative to the initial model, indicating very small sensitivity between these two setups. Model 3 produced 42,357 N, which is 11.0% higher than Model 1 and 9.6% higher than the initial model. These results verify that the Model 3 mesh provides the better total-thrust prediction among the three cases.

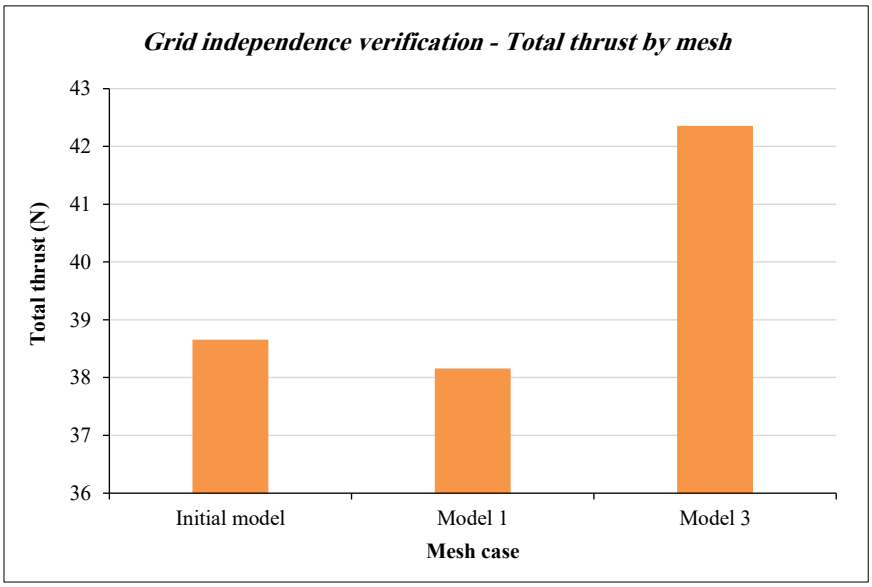

Figure 8. Comparison of initial mode, model 1 and model 3 grids showing convergence behavior of total thrust

4. Post Process Result

In hover, the flow field of the initial configuration shows multirotor features across the six slices: on the upper and lower rotor planes in Figures 9(a) and 9(b), velocity magnitude concentrates in crescent-shaped tip-path footprints with hotspots brushing about 12–15 m/s, while cooler central regions and faint annular lobes reveal gentle inter-rotor shear and early wake merging. The two vertical center planes in Figures 9(c) and 9(d) depict a coherent, symmetric downwash column with wake contraction beneath the disks and little evidence of upstream recirculation, indicating balanced thrust and steady hover trim. The pressure maps on the rotor planes in Figures 9(e) and 9(f) exhibit alternating low/high static-pressure bands aligned with suction/pressure sides, with the strongest gradients over the outer third span and amplitudes within the ±500 Pa scale for both tiers—signalling comparable loading between upper and lower rotors. Overall, the contours confirm tip-dominated loading and a unified downwash that mixes progressively, consistent with the steady RANS with MRF assumption and supportive of the thrust levels reported earlier.

The Model 1 configuration exhibits clear multirotor signatures across all slices in Figures 10(a) to 10(f). On the rotor planes, velocity magnitude concentrates in compact, crescent tip-path footprints with hotspots approaching 12–15 m/s. The upper layer shows slightly more azimuthal asymmetry than the lower layer, where the footprints are more uniform and the inter-rotor shear lobes are better defined toward the center. The vertical center sections as shown in Figures 10(c) and 10(d) reveal a coherent, symmetric downwash column. Jet cores form beneath each disk, contract, and merge into a single plume with progressive mixing, while the region above the vehicle remains near free-stream, indicating little recirculation and a balanced hover trim. Static-pressure maps on the disk in Figures 10(e) and 10(f) display alternating low/high bands aligned with suction/pressure sides, with the strongest gradients located over the outer third of the span and amplitudes contained within the ±500 Pa scale; the upper and lower tiers present comparable patterns, signaling broadly matched loading. Overall, the contours confirm tip-dominated loading, orderly wake contraction, and a unified downwash consistent with the steady RANS with MRF hover assumption for Model 1.

Under hover, Model 3 exhibits a clean, high-energy wake signature across all slices. On the rotor planes in Figures 11(a) and 11(b), the velocity field clusters into compact tip-path crescents with hotspots in the 12–15 m/s band. Compared with the upper layer, the lower layer shows fuller footprints and more continuous inter-rotor streaks, signaling stronger wake merging toward the hub region. The vertical center sections in Figures 11(c) and 11(d) depict four jet cores per tier contracting rapidly and fusing into a single, well-aligned downwash column, while the region above the airframe remains near free-stream—little to no recirculation and a tidy hover trim. Pressure contours on the disks in Figures 11(e) and 11(f) resolve alternating suction/pressure bands with the steepest gradients over the outer third span and amplitudes confined within ±500 Pa for both tiers, evidencing balanced loading between upper and lower rotors. Collectively, the maps indicate tip-dominated lift production, orderly wake contraction, and a coherent plume consistent with the steady RANS with MRF model—behavior that aligns with the higher total thrust obtained for Model 3.

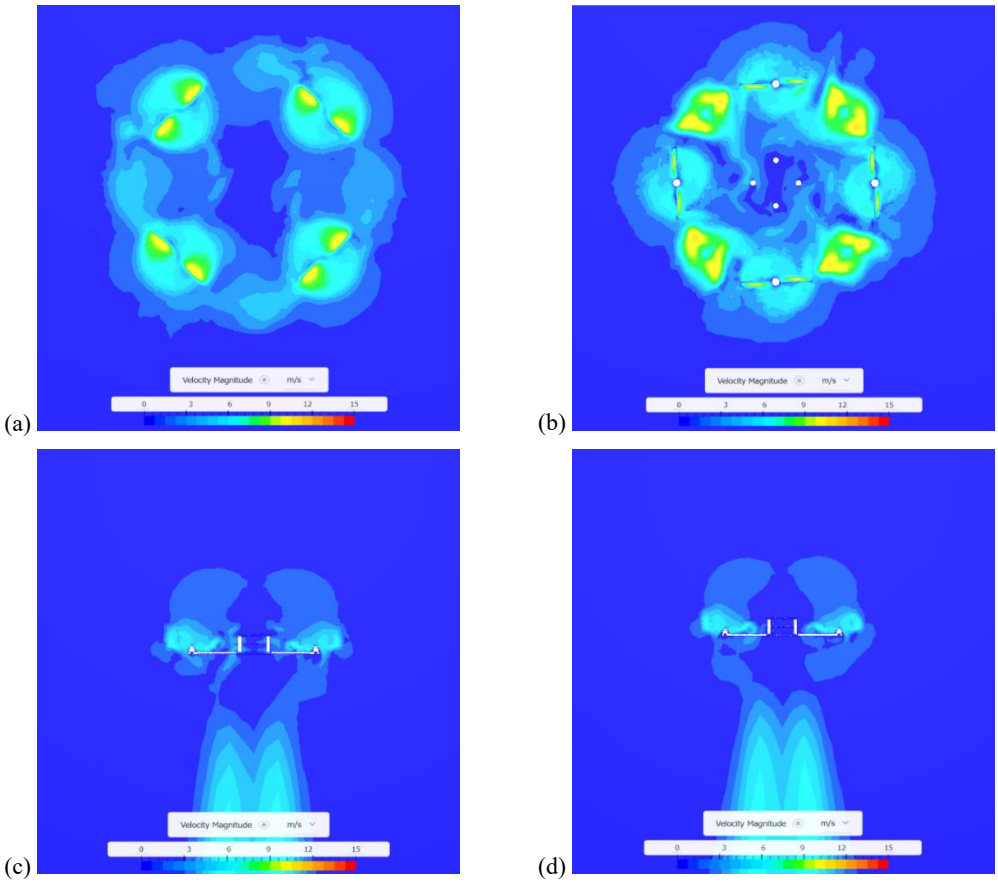

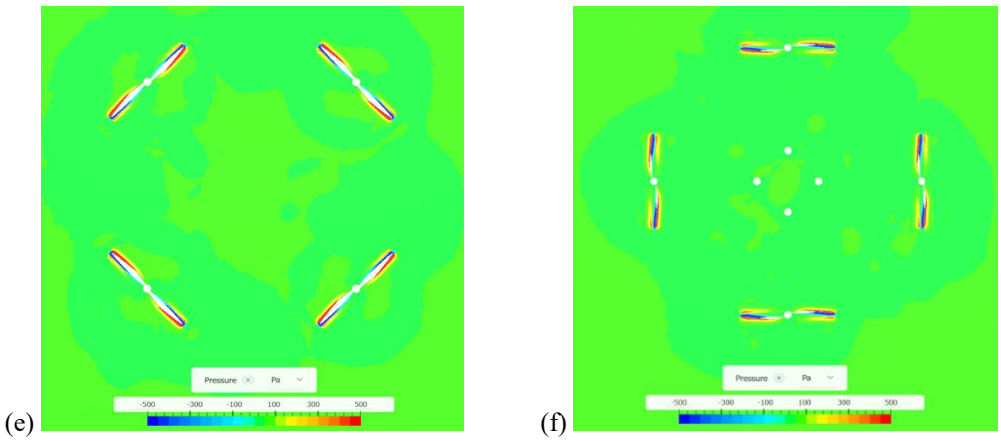

(e) (f)

Figure 9. Baseline octocopter in hover: (a) velocity-magnitude map—upper tier; (b) velocity-magnitude map—lower tier; (c) velocity magnitude on the X–Z centre plane; (d) velocity magnitude on the Y–Z centre plane; (e) pressure contours on upper rotors; (f) pressure contours on lower rotors.

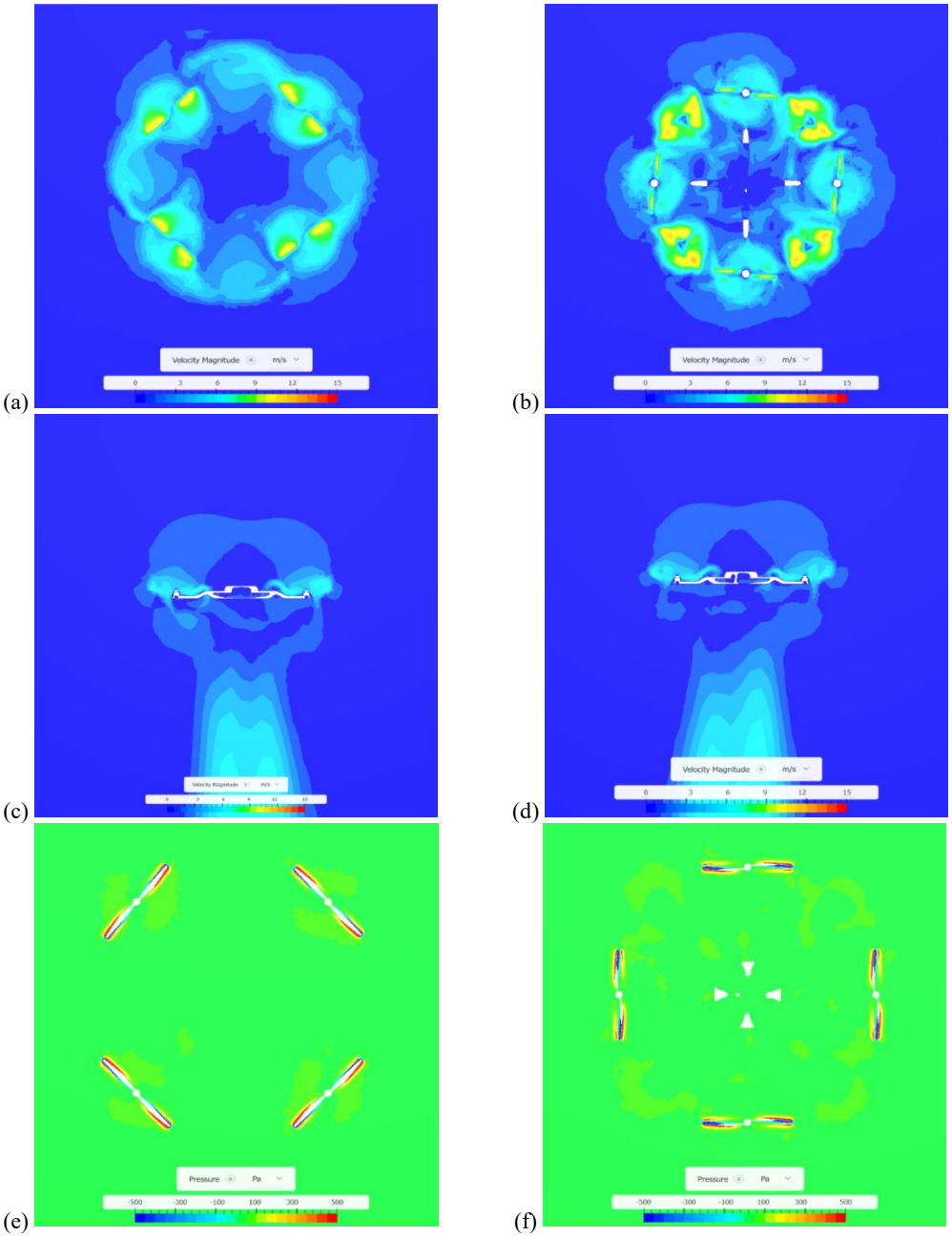

(a) (b)

(c) (d)

(e) (f)

Figure 10. Model 1 in hover: (a) velocity-magnitude map—upper tier; (b) velocity-magnitude map—lower tier; (c) velocity magnitude on the X–Z centre plane; (d) velocity magnitude on the Y–Z centre plane; (e) pressure contours on upper rotors; (f) pressure contours on lower rotors.

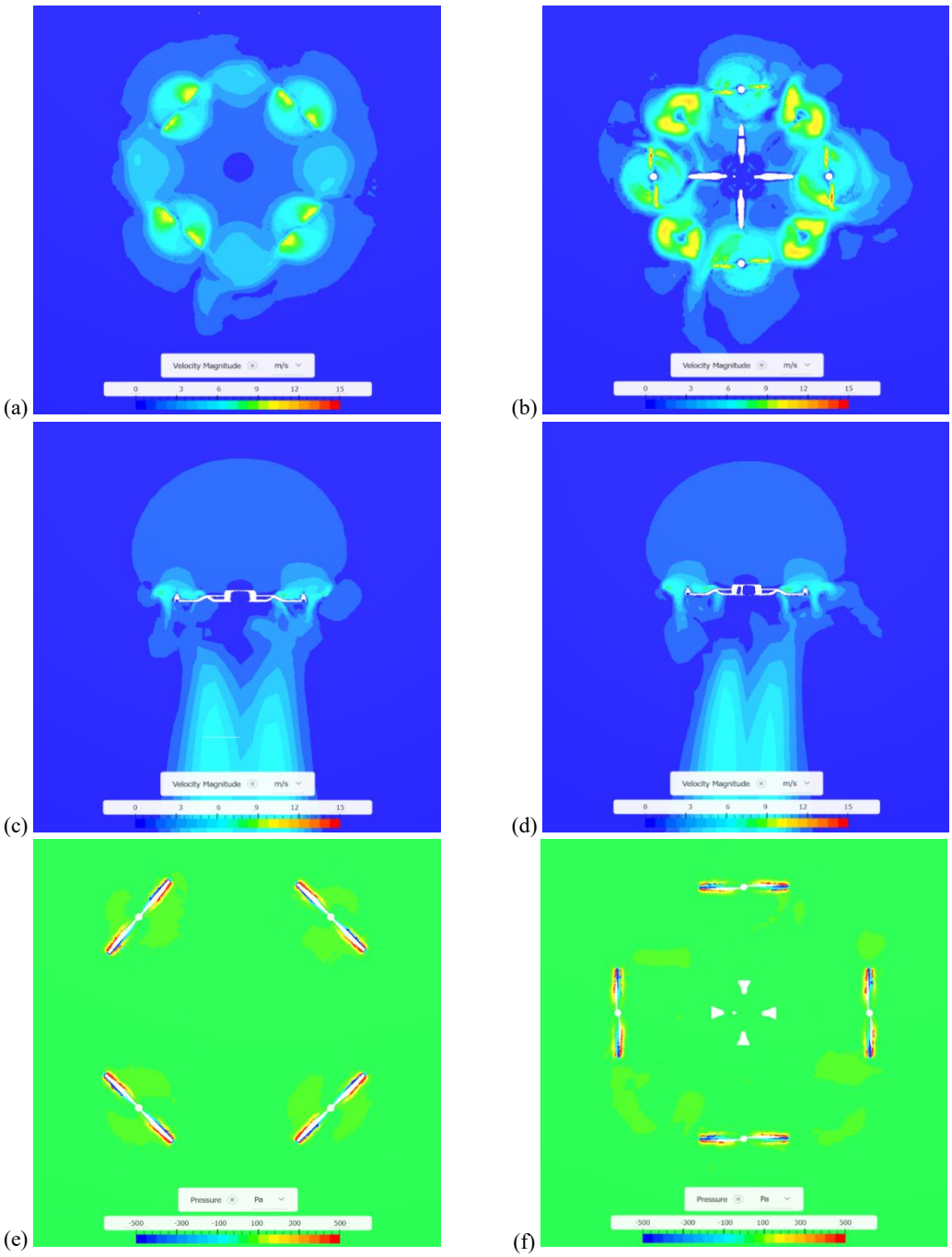

Figure 11. Model 3 in hover: (a) velocity-magnitude map—upper tier; (b) velocity-magnitude map—lower tier; (c) velocity magnitude on the X–Z centre plane; (d) velocity magnitude on the Y–Z centre plane; (e) pressure contours on upper rotors; (f) pressure contours on lower rotors.

4.1. Thrust Analysis

Per-rotor thrust was extracted directly from the CFD force balance using the same steady RANS (SIMPLE) with MRF setup at 4500 RPM for all three meshes: at each iteration the solver integrated pressure and viscous forces over the propeller blade surfaces (and hub), yielding instantaneous thrust for rotors 1–8; the reported values are the mean of the final 20% of samples after residuals and force histories plateaued. The analysis reveals significant differences in thrust generation between the three configurations, as summarized in Figure 12. A consistent trend across all three models was a distinct thrust split between the two tiers. The upper-tier rotors (1–4) generated substantially more thrust than the lower-tier (5–8). This is an expected outcome of the coaxial design, where the upper rotors operate in clean, undisturbed air while the lower rotors must operate in the turbulent downwash. The performance of each model is as follows:

- Initial Model: This baseline configuration produced a total thrust of 38.66 N. The upper-tier rotors (1-4) were clustered in the 6.0-6.25 N range, while the lower-tier (5-8) produced 3.44-3.56 N.
- Model 1: This model produced 38.16 N, a negligible overall thrust decrease of 1.29% compared to the Initial Model. This small change indicates that the generative planar arm design had no significant aerodynamic benefit or penalty.

- Model 3: This model demonstrated the largest performance uplift, generating 42.36 N. This represents a substantial 9.6% thrust increase over the Initial Model and an 11.0% increase over Model 1.

The source of this gain is the key finding. The thrust increase in Model 3 was driven almost entirely by the upper-tier rotors, specifically rotors 1, 2, and 4, which saw performance increases ranging from 13% to 26%. In contrast, the lower-tier rotors 5-7 remained essentially unchanged (Less than or equal to 0.1% shift).

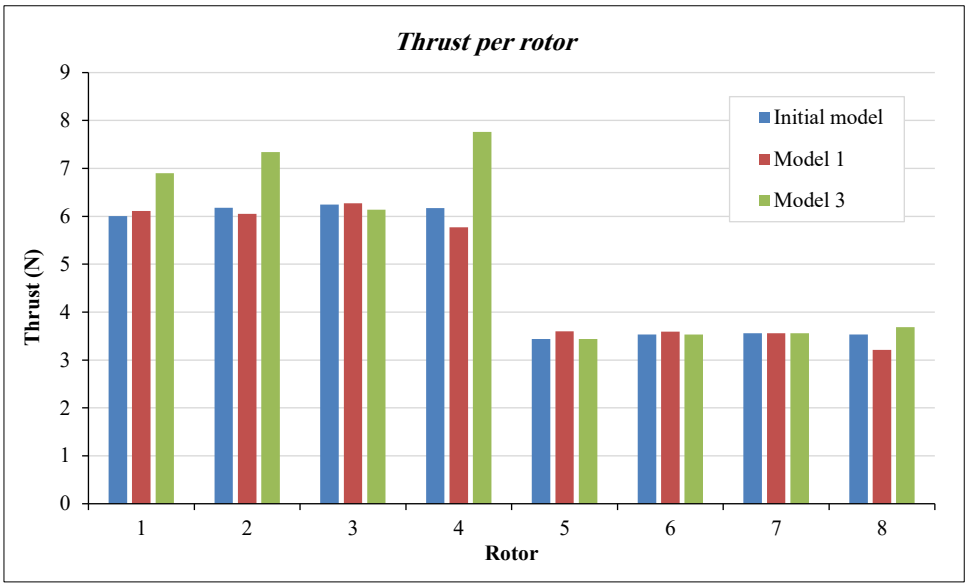

Figure 12. Per-rotor thrust distribution

4.2. Aerodynamic Coefficient and Efficiency Analysis

To provide a standardized comparison of rotor performance independent of operating conditions, three non-dimensional metrics were analyzed: The thrust coefficient (C_T) quantifies the rotor's thrust-generating capability relative to its size and speed. The power coefficient (C_P) quantifies the required shaft power to achieve that thrust (the "cost") and Figure of merit (FM) as a ratio of the two, defines the overall hover efficiency—how effectively the rotor converts input power into useful lift. These parameters are essential for a complete aerodynamic assessment. The whole aerodynamic coefficients and efficiency of three model analysis as shown in Table 3.

Table 3. Aerodynamic performance in hover: non-dimensional coefficients per rotor and mesh configuration

Rotor	Thrust coefficient (C_T)			Power coefficient (C_p)			Figure of Merit *(FM)*		
	Initial model	Model 1	Model 3	Initial model	Model 1	Model 3	Initial model	Model 1	Model 3
1	0.02661	0.02709	0.04058	0.00565	0.0055	0.00866	0.450351	0.499949	0.667475
2	0.02738	0.02682	0.04255	0.00546	0.00566	0.00818	0.481752	0.495729	0.758719
3	0.02769	0.0278	0.04722	0.0055	0.00572	0.00841	0.488173	0.510703	0.862736
4	0.02735	0.02558	0.0544	0.00568	0.00562	0.00936	0.453829	0.470257	0.958534
5	0.01524	0.01596	0.01525	0.00435	0.00457	0.00205	0.282879	0.290495	0.649585
6	0.01564	0.01591	0.01567	0.00434	0.00449	0.0037	0.292946	0.297111	0.374875
7	0.01579	0.01578	0.01579	0.00432	0.00466	0.00366	0.297279	0.284628	0.383334
8	0.01567	0.01423	0.01633	0.00427	0.00439	0.00409	0.29733	0.260151	0.360779

The average C_T for the Initial Model (0.0214) and Model 1 (0.0211) were nearly identical, with Model 1 showing a negligible 1.3% difference. In sharp contrast, Model 3 produced an average C_T of 0.0310, a significant increase of 44.6% over the Initial Model and 46.4% over Model 1. As shown in Figure 13, this system-level gain is attributed to a dramatic performance increase in the upper-tier rotors (e.g., Rotor 4, C_T is 0.0544), while the lower-tier rotors remained consistent with the baseline. This confirms the higher total thrust observed in Model 3 is due to a fundamental improvement in aerodynamic loading on the upper rotors.

The average C_P was similar for the Initial Model (0.0049) and Model 1 (0.0051, a 2.6% increase). Model 3 required significantly more power to achieve its higher thrust, with an average C_P of 0.0060, a 21.5% increase over the Initial Model. This rise is expected and is concentrated in the high-performing upper rotors (e.g., Rotor 4, C_P is 0.0094) as shown in Figure 14, which are doing more aerodynamic work. However, the power coefficient for several lower rotors

in Model 3 decreased (e.g., Rotor 5, C_P *is* 0.0021). This suggests that while the upper rotors are working harder, the lower rotors are operating in a more structured, higher-velocity downwash, which slightly reduces their individual power draw.

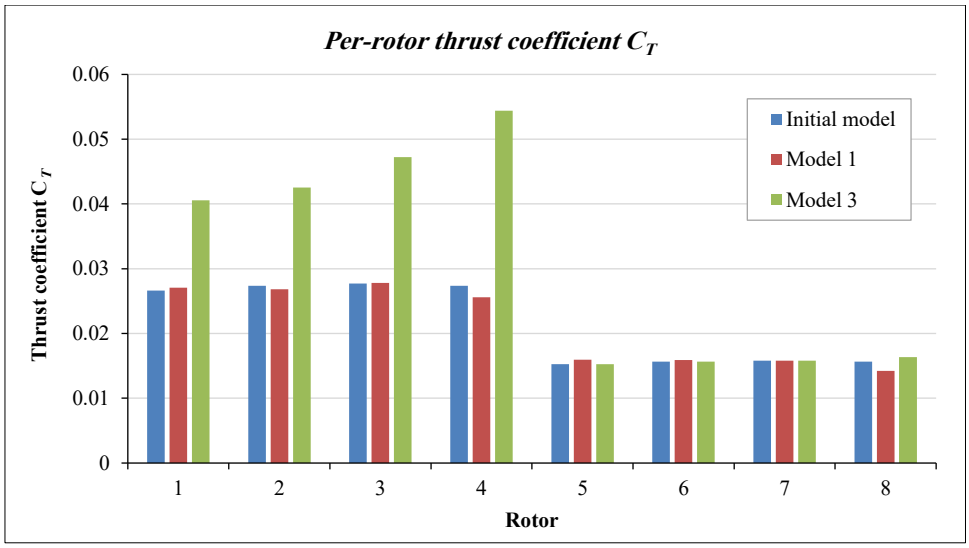

Figure 13. Per-rotor thrust coefficient C_T for the three configurations (Initial model, Model 1, Model 3)

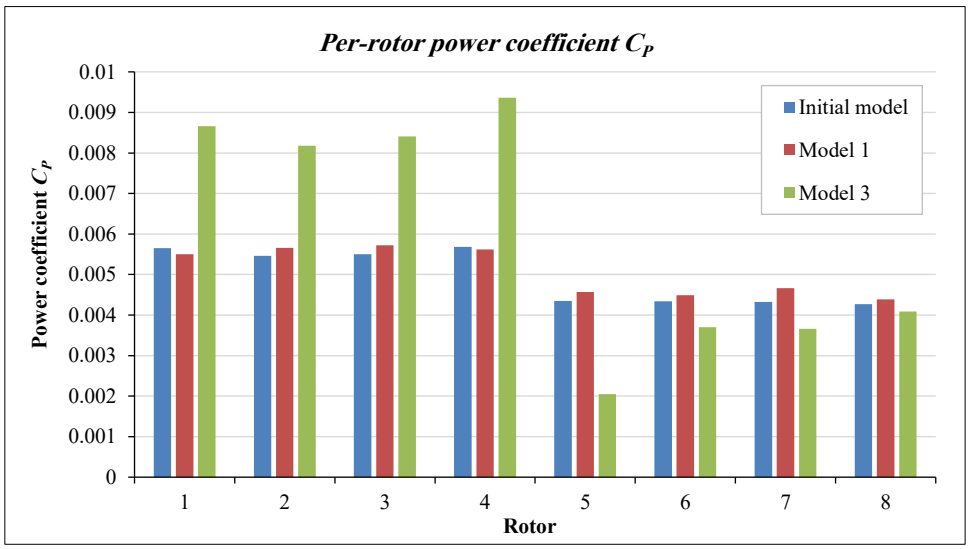

Figure 14. Per-rotor power coefficient C_P for the three configurations (Initial model, Model 1, Model 3)

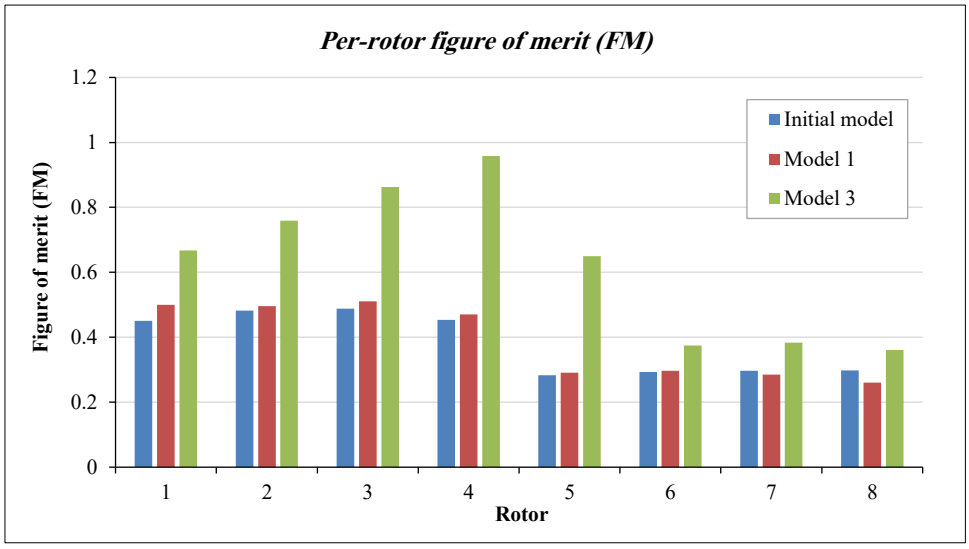

Figure 15. Per-rotor figure of merit (FM) for the three mesh configurations (Initial model, Model 1, Model 3)

Figure of merit (FM) benchmarks how efficiently the system converts shaft power into lift. As shown in Figure 15, the average values progress from 0.3806 for the Initial model to 0.3886 for Model 1, then jump to 0.6270 for Model 3, an improvement of roughly 65% relative to the Initial model. Per-rotor gains are led by the upper tier: rotor 4 is 0.959, rotor 3 is 0.863, rotor 2 is 0.759, and rotor 1 is 0.667. At the same time, the lower-tier rotors also show efficiency improvements; for example, rotor 5 is 0.650 compared with 0.283 in the Initial configuration. In summary, the data demonstrate that the octocopter design of Model 3 does not merely lift more—it lifts smarter, converting shaft power into thrust with substantially higher efficiency.

5. Discussion

This study aimed to clarify how a generative design multirotor frame reshapes hover aerodynamics in a stacked tier arrangement. A standardized steady RANS with MRF hover setup at 4500 RPM was applied to all three geometries, ensuring that observed differences are attributable to configuration rather than modeling settings. The Initial, Model 1, and Model 3 frames used identical 18×7 in propellers with NACA 4412 blade sections, and the generative options retained the same stacked rotor architecture, thereby isolating the influence of frame geometry on inflow development and rotor performance.

A key aerodynamic outcome is the consistent thrust split between the upper and lower tiers. This behavior is consistent with established stacked or coaxial rotor theory. The upper rotor operates in relatively undisturbed inflow, while the lower rotor ingests the contracted wake produced by the upper rotor. That wake typically contains increased axial velocity, residual swirl, and higher turbulence levels, which alters blade loading and reduces the lower rotor thrust for a given rotational speed [4]. The downstream rotor therefore experiences interference-driven induced losses and a reduced thrust-to-power ratio compared with the upstream rotor [5]. As a result, a persistent upper-tier advantage is expected in stacked hover operation, and the trend observed here is a physical consequence of wake ingestion rather than a meshing or solver artifact.

At the system level, Model 3 yields the highest total thrust, reaching 42.36 N. Relative to the Initial and Model 1 frames, this corresponds to improvements of 9.6% and 11.0%, respectively. Flow visualizations support the physical basis of this improvement. The hover wake is tip-dominated and contracts into a coherent downwash, and Model 3 exhibits a clearer, more organized downward jet with reduced recirculation near the airframe. This behavior is consistent with improved inflow quality at the rotor discs and reduced interference losses, and it provides a plausible explanation for the higher total thrust. The 9.6% thrust increase indicates increased payload potential under comparable operating conditions, while the reduced recirculation suggests less energy dissipation into unwanted turbulent mixing.

Non-dimensional performance metrics further clarify the mechanism behind the gains. The thrust coefficient C_T, increases notably for Model 3, largely driven by the upper tier where individual rotors show the strongest loading (for example, Rotor 4 exhibits the highest C_T). In contrast, lower tier C_T remains closer to baseline values, reinforcing that the principal performance improvement is associated with the upper tier inflow and loading environment. The power coefficient, C_P, increases on the highest performing upper rotors, which is expected as these rotors produce more useful aerodynamic work. However, several lower tier rotors in Model 3 show reduced C_P, indicating that the lower tier may operate in a more structured wake with altered inflow conditions that reduce the required power for the same rotation rate. Overall, Model 3 redistributes aerodynamic work across the system, enhancing upper tier performance without proportionally penalizing the lower tier.

These trends are captured by the figure of merit (FM). The system average FM increases from approximately 0.381 (Initial) to approximately 0.389 (Model 1), and then to approximately 0.627 for Model 3, representing an improvement of approximately 65% relative to the Initial frame. Rotor-level FM is highest in the upper tier (for example, Rotor 4 is approximately 0.959), and the lower tier also benefits compared with the baseline (for example, Rotor 5 increases from approximately 0.283 initially to approximately 0.650). These results indicate that Model 3 not only produces greater thrust, but also converts shaft power into useful lift more efficiently under the stacked hover condition.

The magnitude of this FM increase should be interpreted in the context of prior stacked and coaxial rotor studies. Published investigations often report more modest FM changes when varying axial spacing, index angle, or related coaxial parameters, typically on the order of a few percent up to around ten percent, depending on configuration and operating condition [4]. In the present case, the large relative improvement is partly driven by the low baseline FM of the Initial frame (approximately 0.381), which indicates substantial interference and power losses in the stacked arrangement. By contrast, the absolute FM value reached by Model 3 (approximately 0.627) remains within a physically reasonable range for hover efficiency metrics and is consistent with the observed reduction in recirculation and the more coherent downwash field. Therefore, the results suggest that Model 3 enables unusually favorable flow reorganization in the stacked architecture by improving inflow quality and reducing wake confinement and mixing losses, while percentage improvements should be compared cautiously across studies because FM definitions, rotor designs, Reynolds number, and spacing ratios vary between investigations.

This study has several limitations. The steady RANS with MRF formulation provides time-averaged hover loads efficiently, but it does not resolve phase-dependent blade passage effects, wake meandering, or detailed transient vortex dynamics that may occur in stacked rotors. Higher fidelity approaches such as URANS or LES would be required to capture these unsteady mechanisms. In addition, the present analysis is limited to hover conditions. Aerodynamic interactions and performance are expected to change in forward flight due to altered inflow, body induced angles, and wake skew, and future work will extend the analysis to translational regimes.

6. Conclusion

This study designed and evaluated a novel multirotor UAV frame using a generative design workflow and comparative CFD analysis. Three octocopter frames, namely a traditional baseline (Initial) and two generative-design variants (Model 1 and Model 3), were assessed under a common hover methodology using steady incompressible RANS with a pressure-based solver and MRF rotating zones for each rotor, identical 18×7 in propellers with NACA 4412 blade sections, and a matched operating speed of 4500 RPM. A single computational domain and harmonized meshing strategy were applied to all cases, and a grid-independence check confirmed that the key trends were insensitive to mesh density.

The comparative results are clear. Model 3 produced the highest total thrust of approximately 42.36 N, representing increases of 9.6% relative to the Initial configuration and 11.0% relative to Model 1, and it achieved the strongest non-dimensional performance. The thrust coefficient increased notably on the upper tier, the power coefficient increased where greater useful aerodynamic work was produced (with reductions on several lower rotors), and the system-average figure of merit improved from approximately 0.381 (Initial) and 0.389 (Model 1) to approximately 0.627 (Model 3). Flow-field visualizations showed a more coherent, tip-dominated downwash and cleaner inflow to the upper tier, explaining both the thrust gain and the efficiency improvement. Overall, Model 3 is the superior configuration and provides practical guidance for stacked-tier multirotor, indicating that geometries that preserve upper-tier inflow quality and promote an organized combined wake can improve both thrust and hover efficiency.

Based on the study's findings, future work should prioritize addressing the significant aerodynamic interference and thrust imbalance identified between the rotor layers. This could involve investigating design modifications, such as optimizing the vertical separation distance or implementing differential propeller designs (e.g., varying the pitch) for the upper and lower decks. Furthermore, the development of advanced control allocation strategies will be essential to compensate for the observed non-uniform loading. A key next step will be to use the thrust and torque results from this CFD analysis to develop a high-fidelity dynamic model and perform flight simulations in a MATLAB environment. This simulation phase will allow for the design and virtual testing of these control strategies to assess flight stability and performance. Finally, the computational and simulation results must be validated through physical experimentation, which involves fabricating the optimized generative design (Model 3) and performing thrust-stand or wind-tunnel tests to confirm the performance predictions under hover and in forward-flight conditions.

7. Declarations

7.1. Author Contributions

Conceptualization, S.S.; methodology, S.S.; software, S.S.; validation, S.S. and A.C.; formal analysis, S.S.; investigation, S.S.; resources, A.C.; data curation, S.S.; writing—original draft preparation, S.S.; writing—review and editing, S.S. and A.C.; visualization, S.S.; supervision, A.C.; project administration, S.S. and A.C. All authors have read and agreed to the published version of the manuscript.

7.2. Data Availability Statement

The data presented in this study are available on request from the corresponding author.

7.3. Funding and Acknowledgments

The authors acknowledge the financial support provided by the Department of Science and Technology - Science Education Institute (DOST SEI) throughout this study.

7.4. Institutional Review Board Statement

Not applicable.

7.5. Informed Consent Statement

Not applicable.

7.6. Declaration of Competing Interest

The authors declare that they have no known competing financial interests or personal relationships that could have appeared to influence the work reported in this paper.

8. References

[1] Mendu, B., & Mbuli, N. (2025). State-of-the-Art Review on the Application of Unmanned Aerial Vehicles (UAVs) in Power Line Inspections: Current Innovations, Trends, and Future Prospects. Drones, 9(4), 265. doi:10.3390/drones9040265.

[2] Jazairy, A., Persson, E., Brho, M., von Haartman, R., & Hilletofth, P. (2023). Drones in last-mile delivery: a systematic literature review from a logistics management perspective. International Journal of Logistics Management, 36(7), 1–62. doi:10.1108/IJLM-04-2023-0149.

[3] López-Villegas, I., Martínez-Rios, E. A., Izquierdo-Reyes, J., Bustamante-Bello, R., & Falcone, F. (2026). A systematic literature review of emergency communications assisted by unnamed aerial vehicles. Ad Hoc Networks, 182, 104063. doi:10.1016/j.adhoc.2025.104063.

[4] Jeon, S. W., & Lee, S. W. (2025). Effect of Axial Offset, Index Angle, and RPM Differential on the Aerodynamics of Co-Axial Co-Rotating Propellers. Aerospace, 12(10), 940. doi:10.3390/aerospace12100940.

[5] Asper, M., Sirohi, J., & Ricci, M. (2025). Analysis and Testing of Index Angle-Controlled Stacked Rotors in Hover. Journal of the American Helicopter Society, 70(3), 32006. doi:10.4050/JAHS.70.032006.

[6] Aziz, A., Shi, Y., Liu, Y., & Xu, G. (2025). Aerodynamic analysis of rotor-to-rotor interactions in different octocopter configurations. Chinese Journal of Aeronautics, 38(3), 103266. doi:10.1016/j.cja.2024.09.042.

[7] Li, Z., Wu, J., Zhang, P., Wang, L., Chen, L., Zou, Z., & Lin, H. (2025). Layout and Rotation Effect on Aerodynamic Performance of Multi-Rotor Ducted Propellers. Drones, 9(8), 561. doi:10.3390/drones9080561.

[8] Lim, H., Yee, K., & Kim, H. (2025). Flow simulation of propeller-airframe interaction using a modified blade camber surface loading model. Aerospace Science and Technology, 159, 109965. doi:10.1016/j.ast.2025.109965.

[9] Nikolaou, E., Kilimtzidis, S., & Kostopoulos, V. (2025). Winglet Design for Aerodynamic and Performance Optimization of UAVs via Surrogate Modeling. Aerospace, 12(1), 36. doi:10.3390/aerospace12010036.

[10] Kim, J., & Oh, S. (2025). Aerodynamic characteristics of a blended wing body with various winglets. Journal of Mechanical Science and Technology, 39(3), 1201–1210. doi:10.1007/s12206-025-0216-3.

[11] Dayhoum, A., Ramirez-Serrano, A., & Martinuzzi, R. J. (2025). Performance Optimization of Shrouded Rotors: Fixed vs. Variable Pitch in Hover and Forward Flight. Applied Sciences (Switzerland), 15(17), 9594. doi:10.3390/app15179594.

[12] Esakki, B., Raj, P. G., Yang, L. J., Khurana, E., Khute, S., & Vikram, P. (2022). Computational Fluid Dynamic Analysis of Amphibious Unmanned Aerial Vehicle. Journal of Applied and Computational Mechanics, 8(2), 475–484. doi:10.22055/jacm.2020.32461.2018.

[13] Oktay, T., & Eraslan, Y. (2021). Numerical Investigation of Effects of Airspeed and Rotational Speed on Quadrotor UAV Propeller Thrust Coefficient. Journal of Aviation, 5(1), 9–15. doi:10.30518/jav.872627.

[14] He, N. Van, Cong, N. C., & Loi, L. N. (2024). Using CFD To Investigate the Effect of Ducts on Propeller Performance. Journal of Naval Architecture and Marine Engineering, 21(2), 87–101. doi:10.3329/jname.v21i2.37895.

[15] Yildirim, Ş., & Işci, M. (2023). Performance analysis of multi rotor drone systems with changeable rotors. International Review of Applied Sciences and Engineering, 14(1), 45–57. doi:10.1556/1848.2021.00413.

[16] Ahmad, F., Kumar, P., Pravin Patil, P., & Kumar, V. (2021). Design and modal analysis of a Quadcopter propeller through finite element analysis. Materials Today: Proceedings, 46, 10322–10328. doi:10.1016/j.matpr.2020.12.457.

[17] Giljarhus, K. E. T., Porcarelli, A., & Apeland, J. (2022). Investigation of Rotor Efficiency with Varying Rotor Pitch Angle for a Coaxial Drone. Drones, 6(4), 91. doi:10.3390/drones6040091.

[18] Zhu, H., Nie, H., Zhang, L., Wei, X., & Zhang, M. (2020). Design and assessment of octocopter drones with improved aerodynamic efficiency and performance. Aerospace Science and Technology, 106, 106206. doi:10.1016/j.ast.2020.106206.

[19] Sun, J., Yonezawa, K., Tanabe, Y., Sugawara, H., & Liu, H. (2023). Blade Twist Effects on Aerodynamic Performance and Noise Reduction in a Multirotor Propeller. Drones, 7(4), 252. doi:10.3390/drones7040252.

[20] Ahmad, F., Kumar, P., & Patil, P. P. (2021). Analysis of a Pre-Stressed Quadcopter Propeller Using Finite element Approach. Journal of Graphic Era University, 105–120. doi:10.13052/jgeu0975-1416.921.

[21] Intaratep, N., Nathan Alexander, W., Deveport, W. J., Grace, S. M., & Dropkin, A. (2016). Experimental study of quadcopter acoustics and performance at static thrust conditions. 22nd AIAA/CEAS Aeroacoustics Conference, 2016, 2873. doi:10.2514/6.2016-2873.

[22] Balayan, A., Mallick, R., Dwivedi, S., Saxena, S., Haorongbam, B., & Sharma, A. (2024). Optimal Design of Quadcopter Chassis Using Generative Design and Lightweight Materials to Advance Precision Agriculture. Machines, 12(3), 187. doi:10.3390/machines12030187.

[23] Andries, V., & Zaharia, S. M. (2025). Generative Design, Simulation, and 3D Printing of the Quadcopter Drone Frame. Applied Sciences (Switzerland), 15(17), 9647. doi:10.3390/app15179647.

[24] Kowalik, M., Śliwiński, M., & Papis, M. (2025). Utilization of topology optimization and generative design for drone frame optimization. Aircraft Engineering and Aerospace Technology, 97(7), 813–823. doi:10.1108/AEAT-12-2024-0384.

[25] Zhu, H., Nie, H., Wei, X., & Zhang, M. (2022). Design and experimental testing of safe flight control system for novel vertical take-off and landing aircraft. Journal of Vibroengineering, 24(3), 481–500. doi:10.21595/jve.2021.22190.

[26] Sane, S., & Chua, A. (2023). Design and Analysis of a Novel Multirotor Structure Using Generative Design and Finite Element Analysis. 2023 IEEE 15th International Conference on Humanoid, Nanotechnology, Information Technology, Communication and Control, Environment, and Management (HNICEM), 1–5. doi:10.1109/HNICEM60674.2023.10589214.

[27] Palinkas, I., Pekez, J., Desnica, E., Rajic, A., & Nedelcu, D. (2021). Analysis and Optimization of UAV Frame Design for Manufacturing from Thermoplastic Materials on FDM 3D Printer. Materiale Plastice, 58(4), 238–249. doi:10.37358/MP.21.4.5549.

[28] Jacobellis, G., Singh, R., Johnson, C., Sirohi, J., & McDonald, R. (2021). Experimental and computational investigation of stacked rotor performance in hover. Aerospace Science and Technology, 116, 106847. doi:10.1016/j.ast.2021.106847.

[29] Grande, E., Shubham, S., Avallone, F., Ragni, D., & Casalino, D. (2024). Computational aeroacoustic study of co-rotating rotors in hover. Aerospace Science and Technology, 153, 109381. doi:10.1016/j.ast.2024.109381.

[30] ain, D., & Vishwakarma, V. (2024). Investigation of Thrust Performance for Different Drone Propeller Designs Using CFD. Opportunities and Risks in AI for Business Development. Studies in Systems, Decision and Control, 545. Springer, Cham, Switzerland. doi:10.1007/978-3-031-65203-5_27.

[31] Gan, W., Wang, Y., Wang, H., & Zhuang, J. (2024). Aerodynamic Investigation on a Coaxial-Rotors Unmanned Aerial Vehicle of Bionic Chinese Parasol Seed. Biomimetics, 9(7), 403. doi:10.3390/biomimetics9070403.

[32] Pérez, A. M., Lopez, O., & Poroseva, S. V. (2019). Free-Vortex Wake and CFD Simulation of a Small Rotor for a Quadcopter at Hover. AIAA Scitech 2019 Forum. doi:10.2514/6.2019-0597.

[33] Xu, J., Yu, J., Lu, X., Long, Z., Xu, Y., & Sun, H. (2024). Aerodynamic Performance and Numerical Analysis of the Coaxial Contra-Rotating Propeller Lift System in eVTOL Vehicles. Mathematics, 12(7), 1056. doi:10.3390/math12071056.

[34] Xu, A., Wang, F., Chen, M., & Li, L. (2022). Aerodynamic Modeling and Performance Analysis of Variable-Speed Coaxial Helicopter. Applied Sciences (Switzerland), 12(19), 9534. doi:10.3390/app12199534.

[35] Wang, H., Li, G., Li, J., & Zhuang, J. (2025). Aerodynamic Investigation for a Propeller-Induced Lift-Enhancing Vertical Take-Off and Landing (VTOL) Configuration. Drones, 9(1), 20. doi:10.3390/drones9010020.